



Ultrahigh thermal rectification based on near-field thermal radiation between dissimilar nanoparticles

Shizheng Wen^a, Xianglei Liu^{a,b,*}, Sheng Cheng^c, Zhoubing Wang^a, Shenghao Zhang^a, Chunzhuo Dang^a

^aSchool of Energy and Power Engineering, Nanjing University of Aeronautics and Astronautics, Nanjing 210016, China

^bKey Laboratory of Thermo-Fluid Science and Engineering (Xi'an Jiaotong University), Ministry of Education, Xi'an 710049, China

^cChina Nuclear Power Engineering Co, Shenzhen 518000, China



ARTICLE INFO

Article history:

Received 14 April 2019

Revised 26 May 2019

Accepted 27 May 2019

Available online 28 May 2019

Keywords:

Thermal rectification

Nanoparticles

Near-field thermal radiation

ABSTRACT

The capability of manipulating heat flux at the nanoscale has many promising applications in modern electronics and information processing industries. In this paper, a design to achieve ultrahigh thermal rectification is proposed based on near-field thermal radiation between nanoparticles made of intrinsic silicon and a dissimilar material. A record-high rectification ratio of more than 10^4 is theoretically demonstrated, and the underlying mechanism lies in the prominent increase of imaginary part of dielectric function of intrinsic silicon induced by thermally excited electrons at high temperatures. Effects of gap distances, materials and configurations of nanoparticles on the rectification ratio are also investigated. This work may pave the way for the design of efficient thermal diodes, thermal transistors, and other thermotronics devices.

© 2019 Elsevier Ltd. All rights reserved.

1. Introduction

The development of modern electronics and information processing industries depends on the invention of electric diodes, which relies on the rectification of electrons flow. Nevertheless, due to the higher integration of circuits, the heat flux density has increased significantly. Subsequently, a high-temperature working condition may be resulted in, where electronic diodes tend to have low efficiency and even fail. On the other hand, heat flow can also be controlled, which may provide alternative ways to process information at harsh conditions. Thermal rectification is a phenomenon that allows heat flow in a more favorable direction. This phenomenon is promising to pave the way for the realization of future thermal diode/rectifier devices, and thus is attracting extensive attention [1–5].

Previous researches on thermal rectification were based primarily on conduction and convection [6–13]. Alternatively, radiation-based thermal rectifiers, which can avoid contact and intrusion, have been conceived. The performance of thermal rectifier can be characterized by the thermal rectification ratio as

$$R_{\text{ratio}} = \frac{Q_f - Q_r}{Q_r} \quad (1)$$

where Q_f and Q_r represent net heat fluxes in the forward and reverse scenarios, respectively. Otey et al. [14] first proposed a thermal rectifier based on thermal radiation between two plates made of SiC-3C and SiC-6H. They found that the rectification ratio can achieve a maximum value of 0.41 when the gap distance is smaller than $1 \mu\text{m}$, where evanescent waves play a dominant role on the radiative heat transfer [15–35]. Lizuka et al. [36] further improved the rectification ratio to be 0.44 by covering one silicon carbide plate with a dielectric coating. Basu and Francoeur [37] theoretically demonstrated a rectification ratio of 0.51 between silicon films with different doping levels and thicknesses at the temperature between 400 K and 300 K. Ben-Abdallah and Biehs [38] reported a rectification ratio of 0.9 by employing phase-change-driven radiative rectifier. By use of intrinsic bulk silicon and SiO_2 , Wang and Zhang [39] predicted a rectification ratio of 9.9 at the temperature between 300 K and 1000 K at a gap distance of 5 nm. Zhu et al. [40] studied the thermal rectification between two nanoparticles made of SiC-3C and achieved a rectification ratio of 13 with a 26-nm vacuum gap at temperatures between 700 K and 200 K. Nevertheless, radiation-based thermal rectifiers [41–57], as shown clearly in Fig. 1, still have a low rectification ratio compared with conduction-based counterparts (can be as high as 100 [58,59]). Note that the definition of thermal rectification ratio in some references is $\frac{Q_f - Q_r}{Q_f}$ [41,44,48], in order to keep consistence, their results are changed according to Eq. (1). Therefore, investi-

* Corresponding author.

E-mail address: xliu@nuaa.edu.cn (X. Liu).

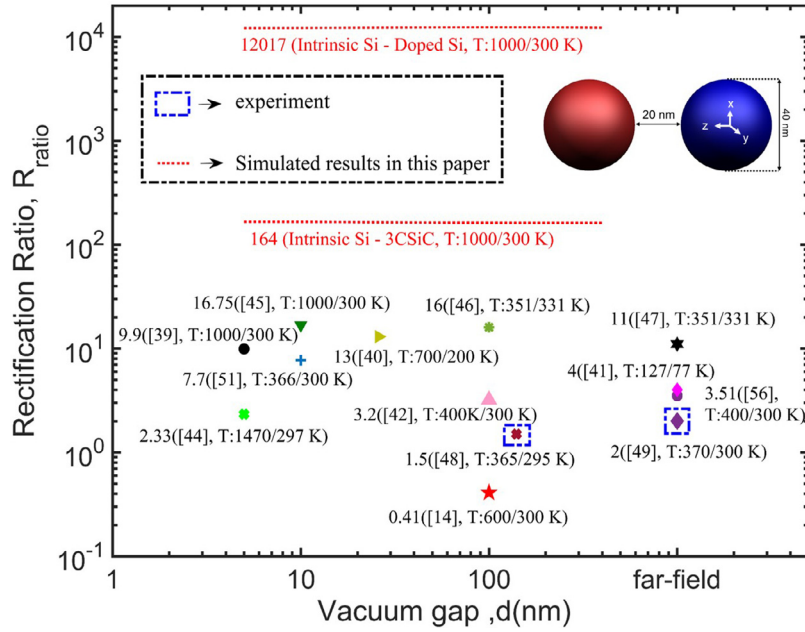


Fig. 1. Variations of thermal rectification ratio with respect to vacuum gap in previous studies and simulated results of the proposed design.

gations on further improving the performance of radiation-based rectifiers are very imperative.

Here, we propose a radiation-based thermal rectifier configured by two nanoparticles made of intrinsic silicon (Si) and a dissimilar material. Its schematic is shown in Fig. 1. Maximum rectification ratios of 165.61 (intrinsic Si – 3C-SiC) and 12,330 (intrinsic Si – doped Si), which are much higher than what reported in previous literature for noncontact thermal rectifiers, are predicted, as the sphere-sphere distance is varied. The underlying mechanism is attributed to the prominent increase of imaginary part of dielectric functions of silicon with temperature. Effects of gap distance, sphere radius, material types, shapes on the rectification performances are discussed.

2. Theory and methods

Silicon has a wide application in microelectronics and semiconductor industries. As a semiconductor material, radiative properties of silicon can be easily tailored by changing temperatures due to thermally excited carriers (electrons). The temperature-dependent dielectric function of silicon is obtained from Fu and Zhang [60], which is valid over a broad temperature ranging from room temperature up to 1000 K. 3C-SiC attracts our attention here because it supports surface phonon polaritons (SPhPs) in the infrared region [61,62]. A classical Lorentz oscillator model $\varepsilon(\omega) = \varepsilon_\infty + \frac{\omega_p^2}{\omega_{TO}^2 - \omega^2 - i\omega\gamma}$ is used to describe the temperature-dependent dielectric function of 3C-SiC [40,61], where $\omega_p^2 = \varepsilon_\infty(\omega_{LO}^2 - \omega_{TO}^2)$, $\omega_{TO} = 149.5 \times 10^{12} - 4.106 \times 10^9(T - 300)$ rad/s and $\omega_{LO} = 182.7 \times 10^{12} - 5.463 \times 10^9(T - 300)$ rad/s are transverse and longitudinal optical phonon frequency, respectively. $\varepsilon_\infty = 6.7 \exp[5 \times 10^{-5}(T - 300)]$, is the high-frequency constant, ω is the angular frequency, the scattering rate $\gamma = 6.6 \times 10^{11} \{1 + 2/[\exp(\hbar\omega_{TO}/2k_B T) - 1]\}$ rad/s.

2.1. Thermal rectification between two spheres

Thermal radiation of objects originates from thermal fluctuations of charge carriers [63]. The spectral poynting vector $E(r_1, \omega) \times H(r_1, \omega)$ at point r_1 outside a body of volume V can be

obtained as [64]

$$\langle E_{i\omega}(r_1, \omega) H_{j\omega}^*(r_1, \omega) \rangle = i\omega\mu_0 \int_V d^3r' \left\{ \bar{G}_E(r_1, r, \omega) \bar{G}_H^*(r_1, r, \omega) \langle J_l(r, \omega) J_m^*(r', \omega) \rangle \right\} \quad (2)$$

where $\bar{G}_E(r_1, r, \omega)$ and $\bar{G}_H(r_1, r, \omega)$ are the dyadic Green's functions (DGFs), which represent the induced electric and magnetic field at position r_1 due to a Dirac delta point source at r . The DGFs, a mathematical technique to solve the Maxwell equation [65], are related to by $\bar{G}_E(r_1, r, \omega) = \nabla_1 \times \bar{G}_H(r_1, r, \omega)$. The “*” denotes the complex conjugate, i and j refer to the three Cartesian components ($i \neq j$), μ_0 is the permeability of vacuum, and $i = \sqrt{-1}$. Integrals are over the region V that contains the fluctuating source. Correlation of fluctuation $\langle J_l(r, \omega) J_m^*(r', \omega) \rangle$ can be described by the fluctuation dissipation theorem (FDT) [66] as

$$\langle J_l(r, \omega) J_m^*(r', \omega) \rangle = \frac{\varepsilon_0 \varepsilon''(\omega) \Theta(\omega, T)}{\pi} \delta_{lm} \delta(r - r') \quad (3)$$

where $\varepsilon''(\omega)$ is the imaginary part of the dielectric function, and ε_0 is the permittivity of vacuum. $\Theta(\omega, T) = \hbar\omega / (e^{\hbar\omega/k_B T} - 1)$ is the mean energy of Planck's oscillator, where $2\pi\hbar$ is Planck's constant and k_B is Boltzmann's constant. δ_{lm} is the Kronecker delta function, $\delta(r - r')$ is the Dirac-delta function. The DGFs of two spheres can be obtained by using the partial-wave scattering method, and are given in [64].

2.2. Near-field thermal radiation between nanoparticles with irregular shapes

For nanoparticles with irregular shapes, analytical expressions of $\bar{G}_E(r_1, r, \omega)$ and $\bar{G}_H(r_1, r, \omega)$ are difficult to find. For this case, the thermal discrete dipole approximation method firstly proposed by Edalatpour and Francoeur is employed [67,68]. The emitter and absorber are discretized into electric dipoles with the number of N_e and N_a , respectively. The volume of each dipole is defined as ΔV_i ($i=1, 2, \dots, N_e+N_a$). a_i is the effective radius of sub-volume i defined as $(3\Delta V_i/4\pi)^{1/3}$. The spectral radiative heat transfer Q_ω , which is equal to the mean energy dissipated in the absorbers ($i=N_e+1$,

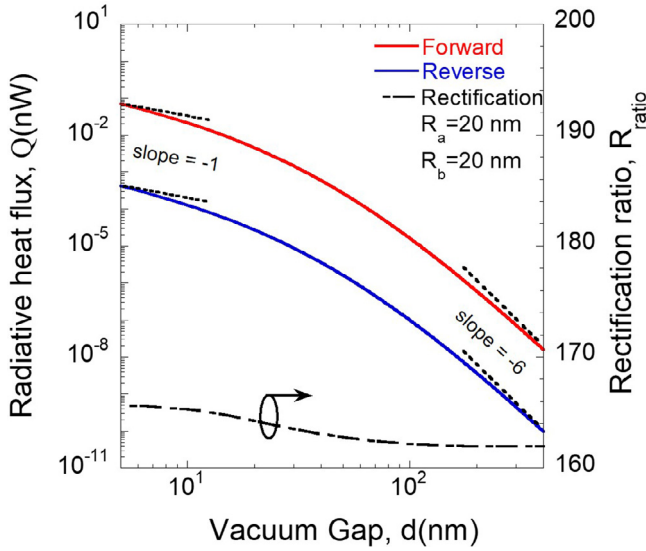


Fig. 2. Near-field radiative heat flux and rectification ratio of the proposed diode as a function of vacuum gap with $R_a = 20\text{nm}$ and $R_b = 20\text{nm}$. The slope of radiative heat flux (in the logarithmic scale) gradually changes from -1 to -6 .

$N_e + 2, \dots, N_e + N_a$) at a given frequency, can be written as [69]

$$Q_\omega = \frac{\omega}{2} \sum_{i=N_e+1}^{N_e+N_a} \left(\text{Im}[(\alpha_i^{-1})^*] \frac{2}{3} k_0^2 \right) \text{tr}(\bar{\bar{R}}_{p_i p_i}) \quad (4)$$

where α_i is referred as the radiative polarizability of dipole i and calculated as [69]

$$\alpha_i = \frac{\alpha_i^{CM}}{1 - \alpha_i^{CM} / 2\pi \epsilon_0 a_i^3 [e^{ik_0 a_i} (1 - ik_0 a_i) - 1]} \quad (5)$$

α_i^{CM} is the Clausius–Mossotti polarizability which is defined as:

$$\alpha_i^{CM} = 3\epsilon_0 \frac{\epsilon_i - 1}{\epsilon_i + 2} \Delta V_i \quad (6)$$

ϵ_i is the dielectric function of dipole i . k_0 is the magnitude of the wavevector in vacuum. The $\text{tr}(\bar{\bar{R}}_{p_i p_i})$ is the trace of the $\bar{\bar{R}}_{pp}$, which is the correlation matrix of the dipole moments P_i and P_j ($i, j = N_e + 1, N_e + 2, \dots, N_e + N_a$). More details about this method can be referred to Refs. [67,70].

3. Results and discussion

3.1. Rectification ratio of the sphere based thermal rectifier

First, we consider a thermal rectifier consisting of two spheres of equal radius made of intrinsic Si and 3C–SiC. For the forward scenario, intrinsic Si is the emitter at $T_h = 1000\text{K}$, and the receiver 3C–SiC is maintained at $T_l = 300\text{K}$. For the reverse scenario, temperatures of intrinsic Si and 3C–SiC are switched. Fig. 2 gives that near-field radiative heat flux (NFRHF) and rectification performance varying with gap distances at the radius R of 20 nm. Because the validity of theoretical framework of fluctuating electrodynamics in the extreme near-field is ambiguous [28,35], range of gap distances starts from 5 nm to 400 nm. As displayed clearly, NFRHF for both forward and reverse scenarios decrease with gap distance increasing due to the reduced contribution of tunneling of evanescent waves. And the descent rate for forward NFRHF (denoted by the red solid line) is close to reverse NFRHF (represented by the blue solid line). The rectification ratio (denoted by the black dash-dotted line) remains almost a constant of 163 with variations of the gap distance. This is in a stark contrast to that of planar

structures whose rectification ratios decrease with gap distance [39,45]. For planar substrate supporting the excitation of surface modes, NFRHF varying with the gap distance tends to follow the law of $1/d^2$, as observed by Refs. [39,45,71] for the forward case. However, for the reverse case, low-temperature intrinsic Si is essential a dielectric thanks to the tiny extinction coefficient [60], as a result, propagating waves inside intrinsic Si have dominant contributions to NFRHF, making it saturated in the deep near field. On the contrary, for nanospheres supporting the excitation of surface modes, NFRHF tend to vary as $1/d$ in the deep near field as discussed in Ref. [72]. When the gap distance is much larger than the sphere radius, both forward and reverse NFRHF vary as $1/d^6$. This is in a good agreement with the dipole approximation, for which two spheres can be considered as dipoles [73,74], and the NFRHT between them can be approximated as [75]

$$Q = \int_0^\infty \frac{3\text{Im}[\alpha_1^{CM}(\omega)]\text{Im}[\alpha_2^{CM}(\omega)]}{4\pi^3 d^6} [\Theta(\omega, T_1) - \Theta(\omega, T_2)] d\omega \quad (7)$$

$\alpha_1^{CM}(\omega)$ and $\alpha_2^{CM}(\omega)$ are the Clausius–Mossotti polarizability of two spheres defined in Eq. (6). Clearly, Q varies as $1/d^6$ according to the dipole approximation, as can be confirmed by Fig. 2. Forward and reverse NFRHF have a similar varying trend with the gap distance at both small and large gap distances, as a result, the rectification ratio does not change much when d varies from 5 nm to 400 nm.

3.2. Rectification mechanism of the sphere-sphere thermal rectifier

In order to unveil the mechanism of high rectification performance of the nanoparticle-based thermal rectifier, spectral radiative heat flux (SRHF) for both forward and reverse scenarios is plotted in Fig. 3(a). Two spheres with the same radius of 20 nm, separated by a vacuum gap of 20 nm, are drawn in the inset. It can be seen that the forward SRHF is much higher than the reverse one for the whole frequency range. The forward NFRHF is two orders of magnitude larger than the reverse one, so the rectification ratio can reach as high as 165. The forward SRHF has two peaks located at angular frequencies of $1.756 \times 10^{14}\text{ rad/s}$ (denoted as Fp1) and $1.771 \times 10^{14}\text{ rad/s}$ (denoted as Fp2), and the reverse SRHF has one peak located at $1.722 \times 10^{14}\text{ rad/s}$ (denoted as Rp1). In order to further explore the source of peaks, we plotted the figure of SRHF between two spheres of identical materials (3C–SiC or intrinsic Si). Fig. 3(b) shows that the SRHF between two 3C–SiC spheres (denoted by the red dash-dotted line) has the same narrow-band characteristic in this region of frequency, and two peaks (denoted as Sp1 and Sp2) are consistent with the forward scenario (Fp1 and Fp2) in Fig. 3(a). Nevertheless, the SRHF between two intrinsic Si spheres (represented by the dotted black line) does not exhibit peaks. That implies that peaks of SRHF in Fig. 3(a) mainly come from radiative properties of 3C–SiC material. And excitation of resonant surface modes can be used to explain it [76]. For the NFRHF between two spheres, the total heat transfer can be divided into different tunnels with different z -components of the angular momentum [40] (coordinate axis in Fig. 1). Different resonant modes of an individual sphere can be labeled with different total angular momentum L . The resonance frequency ω_L of every mode L can be described as [40,76]

$$\text{Re}(\epsilon(\omega_L)) = -\frac{L+1}{L} \quad (8)$$

In the Fig. 3(c), we plot the resonant frequency of 3C–SiC for different modes from 1 to 10 at the temperature of 1000K and 300K. It clearly shows that two peaks of the forward scenario (denoted by Fp1 and Fp2) are coinciding with $L=1$ and $L=2$ modes, and the only peak of the reverse scenario (denoted by Rp1) is in keeping with the $L=1$ mode.

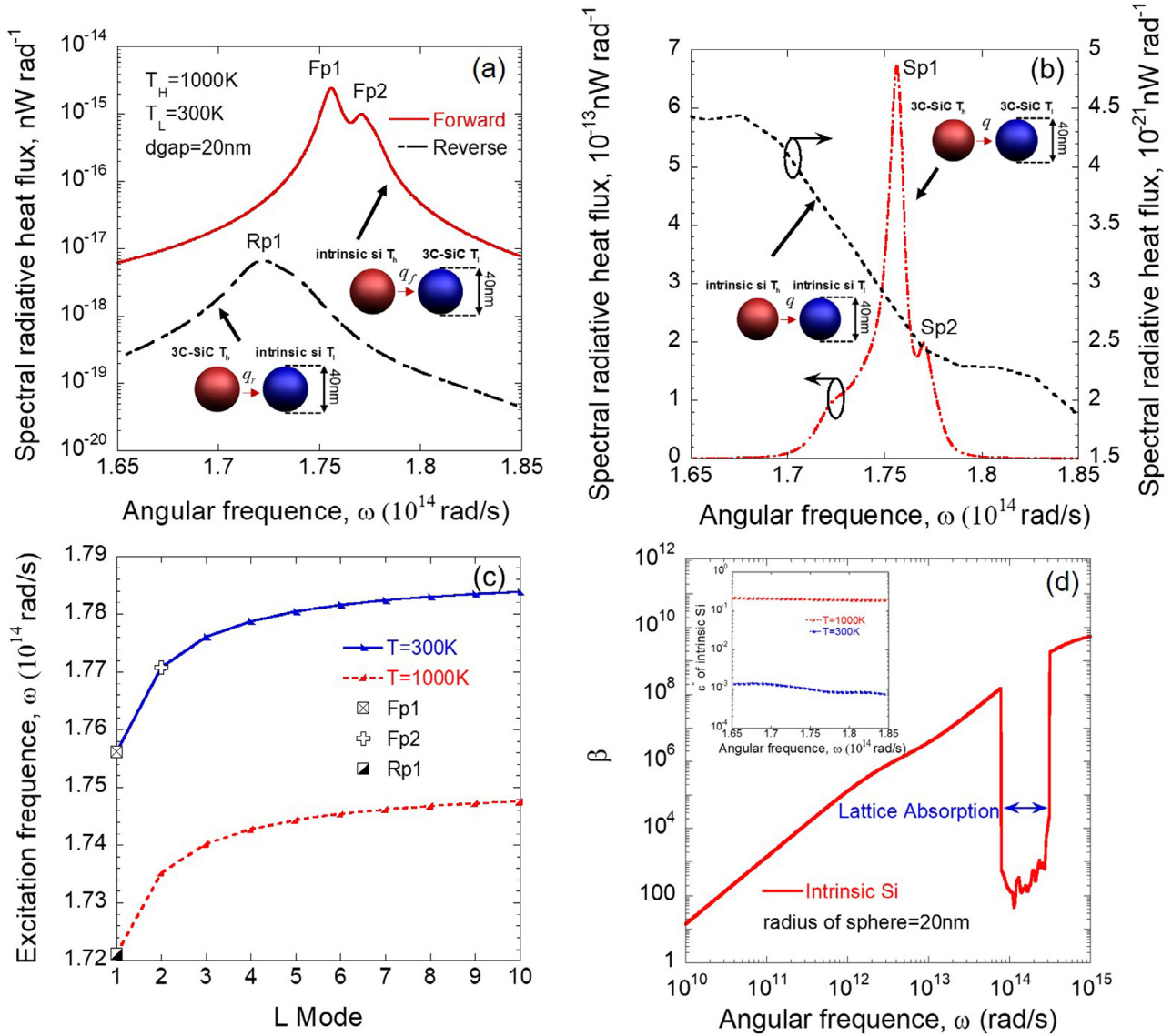


Fig. 3. (a) Forward and reverse spectral radiative heat flux for two spheres made of intrinsic Si and 3C-SiC. (b) Spectral radiative heat flux at vacuum gap = 20 nm between two identical materials made of 3C-SiC or intrinsic Si. (c) Resonant frequencies of different L modes according to the Eq. (8), and frequencies of peaks in Fig. 3(a). (d) The ratio of imaginary part of polarizability β for intrinsic Si varying with angular frequencies. The inset in (d) shows the imaginary part of the dielectric function of intrinsic Si ε'' at the temperature of 300 K and 1000 K, respectively.

Optical properties of Si are sensitive to the temperature. The concentration of thermally excited carriers (electrons) will greatly be improved in high temperatures, which enables Si to become absorbing for low frequencies due to the increasing extinction coefficient κ [60]. The refractive index n changes a little, on the other hand, seldomly changes with the doping level. The relationship $\text{Re}(\varepsilon) = n^2 - \kappa^2$ and $\text{Im}(\varepsilon) = 2n\kappa$ implies the larger imaginary part of the dielectric function of intrinsic Si at higher temperatures, and values of it at 1000 K are almost 100 times that at 300 K, as clearly observed in the inset of Fig. 3(d). As mentioned in session 3.1, rectification ratios are nearly invariable with gap distance, and dipole approximation can be applied to calculate the SRHF when the gap distance is much larger than the sphere radius. The relative difference will be lesser than 10% when gap distances are larger than 100 nm and lesser than 5% for gap distances over 163 nm. Thus, dipole approximation theories can be employed to assist the explanation of the mechanism. In Eq. (7), by using the Eq. (6) and doing some algebraic manipulation, the term $\text{Im}[\alpha^{CM}(\omega)]$ can be

described as

$$\text{Im}[\alpha^{CM}(\omega)] = \frac{12\pi a^3 \varepsilon_0 \varepsilon''}{(\varepsilon' + 2)^2 + (\varepsilon'')^2} \quad (9)$$

where ε' is the real part of the dielectric function, ε'' is the imaginary part of that. For both forward and reverse scenario, the imaginary part of dielectric function of intrinsic Si is negligible compared with the real part of dielectric function, so the term $(\varepsilon'')^2$ in the denominator of Eq. (9) can be removed, the form of Eq. (9) can be further simplified as $\text{Im}[\alpha^{CM}(\omega)] = 12\pi a^3 \varepsilon_0 \varepsilon'' / (\varepsilon' + 2)^2$. Clearly, $\text{Im}[\alpha^{CM}_{\text{intrinsic Si}}(\omega)]$ is proportional to the imaginary part of dielectric function of intrinsic Si, which gives rise to $\text{Im}[\alpha^{CM}_{\text{intrinsic Si}}]$ at 1000 K is also 100 times that at 300 K. Meanwhile, the imaginary part of polarizability of intrinsic Si, which changes little at this region from 1.65×10^{14} rad/s to 1.85×10^{14} rad/s, can be viewed as independence of frequency. Therefore, the term $\text{Im}[\alpha^{CM}_{\text{intrinsic Si}}(\omega)]$ in Eq. (7) can be taken in

front of the integral symbol and the equation can be described as

$$Q = \frac{3\text{Im}[\alpha_{\text{intrinsic Si}}^{\text{CM}}]}{4\pi^3 d^6} \times \int_{1.65 \times 10^{14} \text{ rad/s}}^{1.85 \times 10^{14} \text{ rad/s}} \text{Im}[\alpha_{\text{3C-SiC}}^{\text{CM}}(\omega)] \times [\Theta(\omega, T_1) - \Theta(\omega, T_2)] d\omega \quad (10)$$

Due to the reason that $\text{Im}[\alpha_{\text{3C-SiC}}^{\text{CM}}(\omega)]$ changes a little with temperatures, NFRHF according to Eq. (10) is mainly dominated by $\text{Im}[\alpha_{\text{intrinsic Si}}^{\text{CM}}]$, resulting in the fact that the rectification ratio is determined by the ratio of it. That explains the high-performance of thermal rectifier between intrinsic Si and 3C-SiC. In order to further exploit the potentiality of thermal rectifier between intrinsic Si and a dissimilar material, Fig. 3(d) gives the ratio of polarizability for intrinsic Si ($\beta = \text{Im}[\alpha_{\text{intrinsic Si}}^{\text{CM}}(\omega)]_{1000\text{K}} / \text{Im}[\alpha_{\text{intrinsic Si}}^{\text{CM}}(\omega)]_{300\text{K}}$) varying with angular frequencies. As displayed in the figure, β increases with rising angular frequencies due to the smaller value of $\text{Im}[\alpha_{\text{intrinsic Si}}^{\text{CM}}(\omega)]_{300\text{K}}$. Interestingly, a sharp decline of β can be observed between $7.87 \times 10^{13} \text{ rad/s}$ and $3.22 \times 10^{14} \text{ rad/s}$. For intrinsic Si at 300 K, lattice absorption occurs in the mid infrared and introduces some absorption for $7.87 \times 10^{13} \text{ rad/s} < \omega < 3.22 \times 10^{14} \text{ rad/s}$. Subsequently, the extinction coefficient κ of intrinsic Si will be greatly improved, resulting in the fact that $\text{Im}[\alpha_{\text{intrinsic Si}}^{\text{CM}}(\omega)]$ will not increase dramatically in the region when the temperature rises from 300 K to 1000 K [60]. Consequently, for nanoparticle-based thermal rectifiers made of intrinsic Si and a dissimilar material, rectification ratios will further be improved if the excitation frequency of a dissimilar material is away from the region of lattice vibrations for intrinsic Si.

In Fig. 4(a) and (b), we plot the SRHF for the forward scenario at different radii of intrinsic Si and 3C-SiC spheres, respectively. In Fig. 4(a), the SRHF at every frequency increases with Si spheres' radius, but dominated resonant frequencies almost do not change. Whereas, Fig. 4(b) clearly shows that blue-shift appears on the dominated resonant frequency with increasing radii of 3C-SiC spheres. This just verifies what we have proposed before that the peak is induced by the excitation of surface modes of the 3C-SiC, and increasing the radius of Si sphere simply enhances the SRHF at each frequency due to the larger area that two spheres are facing. In Fig. 4(b), we also plot the peak position (denoted by the green line) of SRHF for the plate-plate structure with the same material pair and temperature differences as the forward scenario. Interestingly, with the increasing radius of R_b , the dominated peak of two spheres system will get close to that of plate-plate systems ($1.781 \times 10^{14} \text{ rad/s}$). This can be easily comprehended by the configuration of the rectifier when changing the radius of R_b . It will approximate the NFRHF between a sphere (Si) and a plate (3C-SiC) when the R_b tends to be infinite, and the resonant frequency of surface modes of the 3C-SiC material will be characterized by the plate structure ($\text{Re}(\varepsilon(\omega)) \approx -1$) [77]. That is why we observe that increasing the radius of 3C-SiC makes a gradual transition of excitation condition of surface modes from the frequency determined by the configuration of sphere (localized surface modes) to the configuration of plate (propagating surface modes).

3.3. Optimization of thermal rectification of nanoparticles

In order to further enhance the near-field thermal rectification ratio of nanoparticles, we optimized parameters which are related to the rectifier. In Fig. 5(a), we plot the rectification ratio for a given set of temperature bias as specified by T_h and T_l , with $T_h > T_l$. It can be seen that the ultrahigh rectification ratio ($R_{\text{ratio}} > 100$) is mainly concentrated in the region of $T_h > 600\text{K}$ and $T_l < 600\text{K}$, while the rectification ratio close to the diagonal line ($T_h = T_l$) is smaller. As mentioned in the session 3.2, the mechanism of high

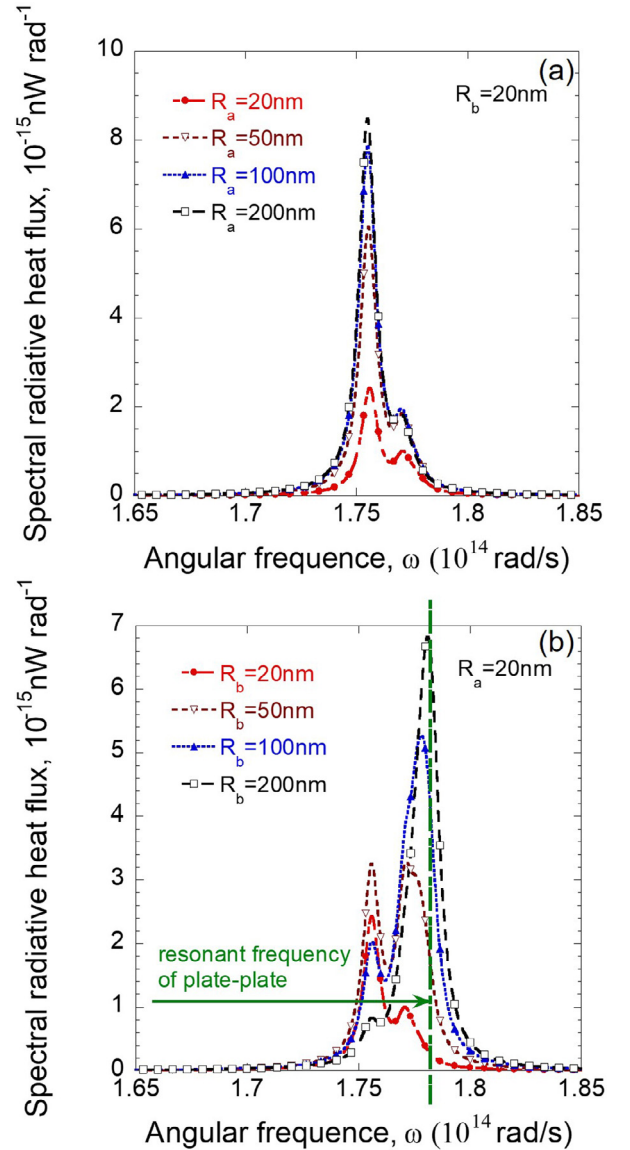


Fig. 4. (a) Spectral radiative heat flux of spheres with Si radius R_a of 20, 50, 100, 200 nm at the gap of 20 nm. (b) Spectral radiative heat flux of spheres with 3C-SiC radius R_b of 20, 50, 100, 200 nm at the gap of 20 nm.

rectification ratios is due to the prominent increase of imaginary part of dielectric function of intrinsic Si. Therefore, it is expected that larger temperature differences lead to better rectification performances, as can be confirmed in Fig. 5(a). Only when T_h is higher than 600 K, the imaginary part of dielectric function of intrinsic Si is high enough to make thermal radiation of intrinsic Si has a good match with that of 3C-SiC [39,60]. It can be easily confirmed in the inset of Fig. 5(a), which shows the rectification ratio varying with T_h with T_l set as 300 K. The rectification ratio magnitude as a function of intrinsic Si sphere radius R_a and 3C-SiC sphere radius R_b are plotted in Fig. 5(b). Due to the fact that the dielectric function of nanoparticles will deviate from that of the bulk when the size is smaller than 10 nm [78], the range of sphere radius is limited from 10 nm to 100 nm. The figure shows that there is an increase of the rectification ratio when the radius of 3C-SiC and intrinsic Si is large and small, respectively. The diagonal line of Fig. 5(b) corresponds to the case where two bodies have equal radii, and the rectification ratio is generally small in the region of $R_a > R_b$. In order to reveal the phenomenon, we plot the SRHF of spheres with 3C-SiC

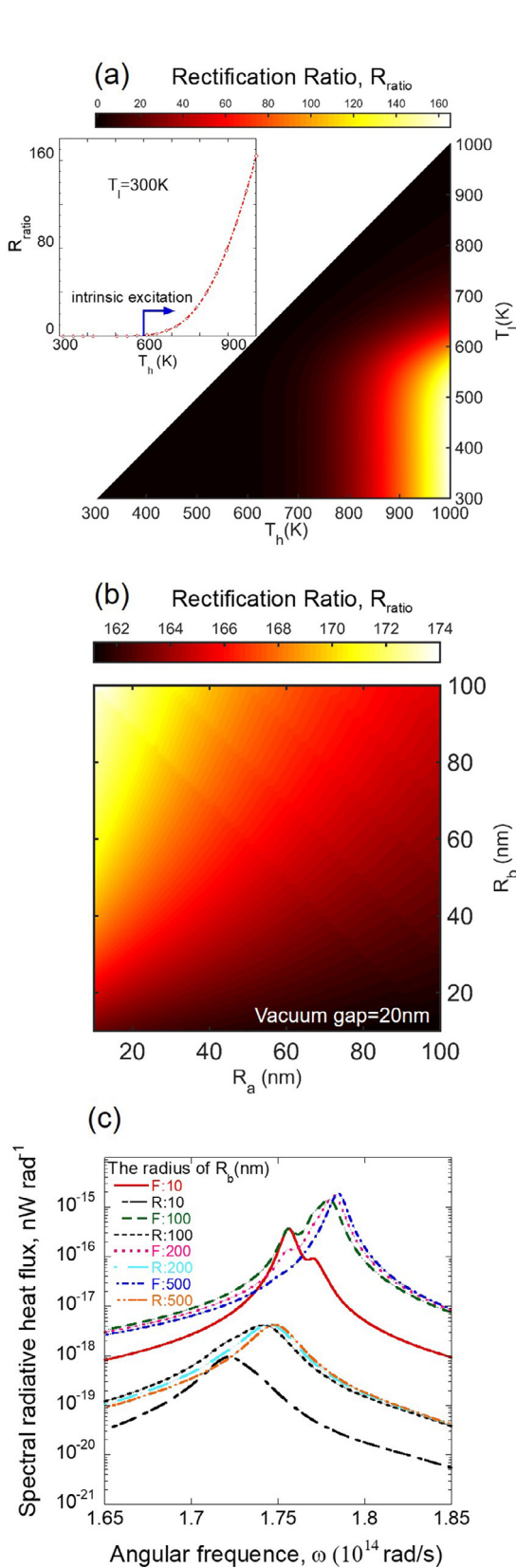


Fig. 5. Rectification ratio as a function of (a) the Si sphere temperature T_h and 3C-SiC sphere temperature T_l ; (b) the Si sphere radius R_a and 3C-SiC sphere radius R_b ; (c) Spectral radiative heat flux of spheres with 3C-SiC radius R_b of 10, 100, 200, 500 nm at vacuum gaps of 20 nm and R_a of 10 nm for the forward and reverse scenario.

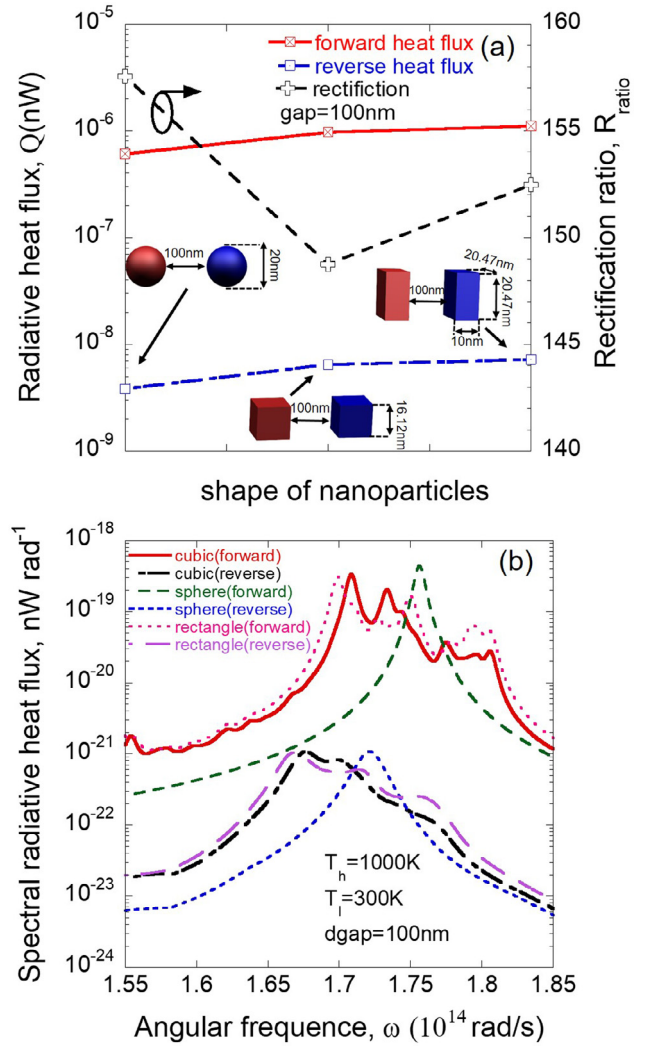


Fig. 6. (a) The forward and reverse radiative heat flux and rectification ratio for the configuration of sphere-sphere, cube-cube, and rectangle-rectangle, which has the equal volume. (b) The forward and reverse spectral radiative heat flux between two cubes, two spheres, and two rectangles made of intrinsic Si and 3C-SiC separated by a 100 nm gap.

radius R_b of 10, 100, 200, 500 nm at vacuum gap of 20 nm and R_a of 10 nm for both forward and reverse scenarios, as shown clearly in Fig. 5(c). When the radius of R_b is larger than 100 nm, it can be seen that the width of the peak for the forward SRHF decreases while its height increases. However, for the reverse case, the peak width decreases while its height almost does not change. This has given rise to the fact that the decrease of forward NFRHF is slower than the reverse counterpart with a large R_b . Therefore, the rectification ratio can be further enhanced when the rectifier approach the configuration consisting of an intrinsic Si sphere and a 3C-SiC plate.

We also discuss the thermal rectification between two nanoparticles of different shapes. In order to eliminate the effect of volume and distance, three configurations are all separated by a distance of 100 nm and have the equal volume. Spheres have the radius of 20 nm, cubes have side lengths of 16.12 nm, and rectangles have the length of $20.47 \times 20.47 \times 10$ nm. Fig. 6(a) gives the NFRHF (calculated with T-DDA [67]) and rectification performance considering different shapes of nanoparticles. Here, we set 1000 sub-volumes for a single subject, and results of NFRHF for three rectifiers achieve convergence [70]. The sphere-sphere configuration is

Table 1
Ten different material pairs used for constituting thermal rectifiers.

Numbers	Material pairs	Numbers	Material pairs
1	Intrinsic Si - Doped Si (10^{18} cm^{-3})	6	Doped Si (10^{18} cm^{-3}) - SiO_2
2	Intrinsic Si - 3C-SiC	7	Doped Si (10^{18} cm^{-3}) - Au
3	Intrinsic Si - SiO_2	8	3C-SiC - SiO_2
4	Intrinsic Si - Au	9	3C-SiC - Au
5	Doped Si (10^{18} cm^{-3}) - 3C-SiC	10	SiO_2 - Au

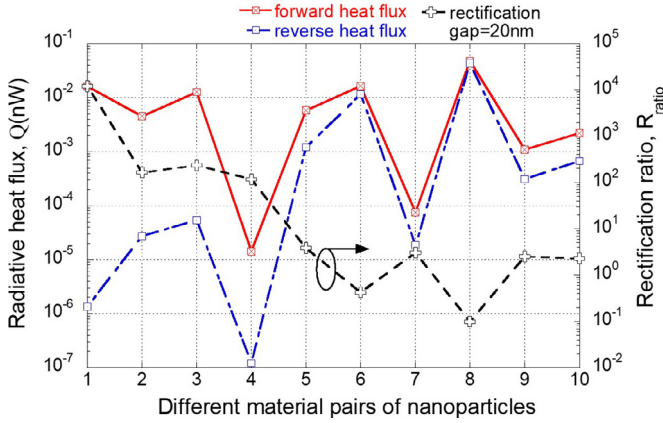


Fig. 7. Near-field radiative heat flux and rectification ratio of the proposed diode with $R_a = 20\text{nm}$ and $R_b = 20\text{nm}$ for different material pairs (numbers on the abscissa axis are consistent with those in Table 1).

shown to have the highest rectification ratio of 157 (denoted by the black dashed line) among three rectifiers, while the cubic-cubic system has the smallest one of 148. The rectangle-rectangle rectifier has a medium rectification ratio of 152. Meanwhile, as denoted by the red and blue line, respectively, both forward and reverse NFRHF increase when changing the configuration of sphere-sphere to rectangle-rectangle. The reason lies in not only a larger cross area (two nanoparticles are facing) but also broader radiative heat transfer spectrum as shown in Fig. 6(b). Reverse NFRHT increases more prominently compared with the forward counterpart when particle shape changes to cubes or rectangles, as a result, spheres have the highest rectification performance. It can be seen from Fig. 6(b) that SRHFs for both non-spherical particles are complex and have more than one peak. This is not surprising given surface resonance frequencies are well-known to heavily depend on the shape/size of the small particle [76]. Presence of multiple resonance peaks further explain higher NFRHT of non-spherical particles for both forward and reverse scenarios as shown in Fig. 6(a).

3.4. Effects of materials' choice on thermal rectification of nanoparticles

To further explore effects of materials' choice on the rectification performance, we calculate rectification ratios of ten different material pairs shown in Table 1. The dielectric function of Au and SiO_2 can be found in the Ref. [39]. Fig. 7 gives the NFRHF and rectification performance of two nanospheres with different material pairs while maintaining the radius at 20nm. Numbers on the abscissa axis are consistent with those in Table 1. As shown in Fig. 7, it is not difficult to find that rectification ratios are all above 100 when intrinsic Si is included in the material pair (See numbers 1, 2, 3, 4). For material pairs 2 and 3, both forward and reverse SRHFs have narrow-band characteristics and the excitation frequency of 3C-SiC or SiO_2 is located in the region of lattice vibration for intrinsic Si. The high rectification ratio agrees well with β in Fig. 3(d), as mentioned in session 3.2. For material pair 1, the

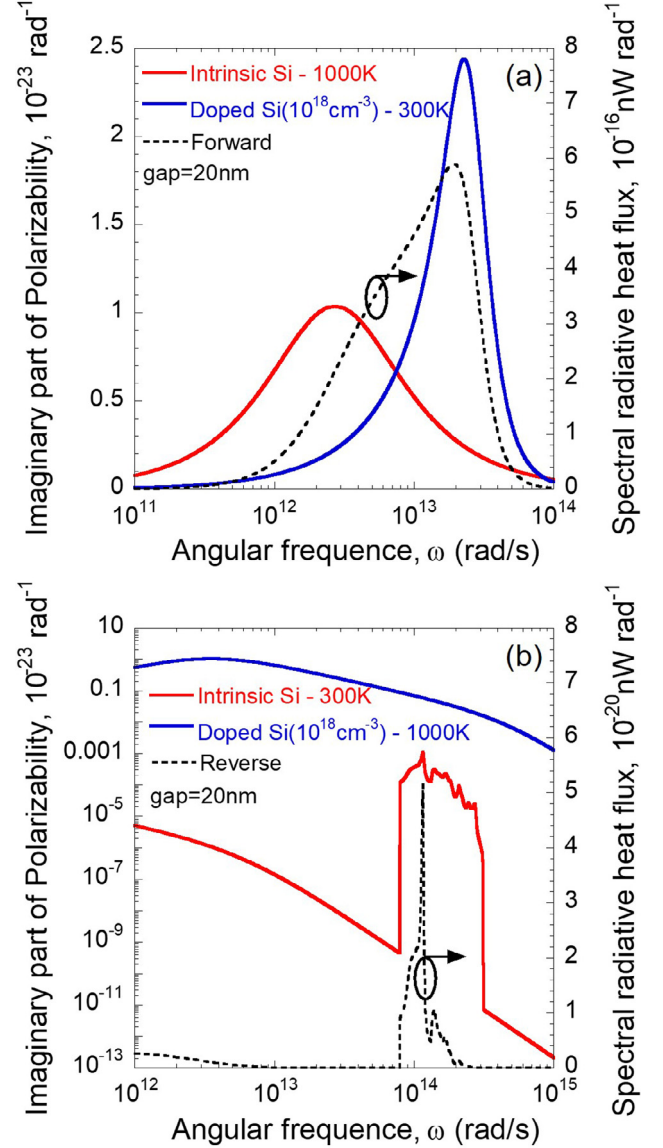


Fig. 8. Spectral radiative heat flux and imaginary part of polarizability for intrinsic Si and doped Si (10^{18} cm^{-3}) in the (a) forward scenario; (b) reverse scenario.

rectification ratio can even reach more than 10^4 . In order to unveil the mechanism of it, both forward and reverse SRHFs and imaginary part of polarizability for two materials are plotted in Fig. 8(a) and (b), respectively. In the forward biased case, the carrier concentration of intrinsic Si at 1000K will have nearly the same value as that in doped Si (10^{18} cm^{-3}) at 300K [60], resulting in the similar dielectric function of the emitter and the receiver. Therefore, $\text{Im}[\alpha^{\text{CM}}(\omega)]$ for two materials will have a strong match and subsequently a large heat transfer enhancement will occur, as clearly observed in Fig. 8(a). In the reverse biased case, $\text{Im}[\alpha^{\text{CM}}(\omega)]$ of

doped Si (10^{18} cm^{-3}) at 1000 K will merely match the peak induced by absorption of lattice vibration for intrinsic Si at 300 K, and the NFRHF is extremely small. Thus, A record-high rectification ratio of more than 10^4 is theoretically achieved. In addition, effects of gap distance for rectification ratios between intrinsic Si and doped Si are also verified to be independent of the gap, as observed in Fig. 1. For material pair 4, due to the mismatch of polarizability between intrinsic Si and Au for the forward scenario, thermal rectification ratios are only dominated by the enhancement of polarizability for intrinsic Si and only reach more than 100. The temperature dependence of dielectric functions of other materials is not so prominent as that of intrinsic Si, as a result, their rectification ratios are less than 5. Melting points of these materials (Si: 1687 K, 3C-SiC: 3103 K, SiO_2 : 1986 K, Au: 1337 K) are all above 1000 K. Besides, the heat flux of 19.73 W/cm^2 between intrinsic Si and doped Si at the gap of 5 nm, can be dissipated by current cooling techniques [79] in order to maintain the temperature difference of the system. Therefore, the proposed thermal rectifier in this paper can reliably perform. As for the experimental realization, two nanoparticles can be put on a substrate with a very low thermal conductivity in the vacuum environment, so that heat transfer between aforementioned nanoparticles is still governed by near-field thermal radiation. Therefore, the ultrahigh rectification performance can be maintained.

4. Conclusion

In summary, a highly efficient radiative thermal rectifier consisting of two nanoparticles, i.e., intrinsic Si nanoparticle and a dissimilar nanoparticle, is proposed in this paper. Due to the thermal excitation of electrons of intrinsic Si at high temperature, the proposed rectifier can possess a high rectification ratio over 100. Particularly, for the nanoparticles comprising by intrinsic Si and doped Si (10^{18} cm^{-3}), the rectification ratio can reach a record-high value of more than 10^4 . This is because thermal radiation for the forward scenario is greatly enhanced due to a strong match of polarizabilities, resulting from the similar carrier concentration of the intrinsic Si at 1000 K and doped Si (10^{18} cm^{-3}) at 300 K. Also, the rectification ratio is insensitive to the variation of distances between two nanoparticles. Peaks of the thermal radiation spectrum and rectification ratios can be regulated by changing the shape of nanoparticles, which provides an additional way to tune the rectification performance. This work paves the way for the design of more efficient thermal rectifiers, and promotes the development of noncontact thermotronics.

Acknowledgements

This work is mainly supported by National Natural Science Foundation of China (grant nos. 51706096 and 51820105010). The authors also want to acknowledge the support from Fundamental Research Funds for the Central Universities (grant no. 56XIA17001) and Foundation of Key Laboratory of Thermo-Fluid Science and Engineering (Xi'an Jiaotong University), Ministry of Education (KLTFS2016KF03).

References

- [1] Wehmeyer G, Yabuki T, Monachon C, Wu J, Dames C. Thermal diodes, regulators, and switches: physical mechanisms and potential applications. *Appl Phys Rev* 2017;4(4):041304.
- [2] Ben-Abdallah P, Biehs S-A. Thermotronics: towards nanocircuits to manage radiative heat flux. *J Phys Sci* 2017;72(2):151–62.
- [3] Chang C, Okawa D, Majumdar A, Zettl A. Solid-state thermal rectifier. *Science* 2006;314(5802):1121–4.
- [4] Ben-Abdallah P, Biehs S-A. Contactless heat flux control with photonic devices. *Aip Adv* 2015;5(5):053505.
- [5] Sadat H, Le Dez V. Thermal rectification in a bilayer wall: coupled radiation and conduction heat transfer. *Appl Therm Eng* 2016;107:1248–52.
- [6] Roberts NA, Walker DG. A review of thermal rectification observations and models in solid materials. *Int J Therm Sci* 2011;50(5):648–62.
- [7] Globe S. Natural-convection heat transfer in liquids confined by two horizontal plates and heated from below. *Trans ASME* 1959;81(1):24–8.
- [8] Roberts NA, Walker DG. Computational study of thermal rectification from nanostructured interfaces. *J Heat Trans* 2011;133(9):092401.
- [9] Yang N, Zhang G, Li B. Thermal rectification in asymmetric graphene ribbons. *Appl Phys Lett* 2009;95(3):033107.
- [10] Thomas T, Probert S. Thermal contact resistance: the directional effect and other problems. *Int J Heat Mass Transfer* 1970;13(5):789–807.
- [11] Zhu J, Hippalgaonkar K, Shen S, Wang K, Abate Y, Lee S, et al. Temperature-gated thermal rectifier for active heat flow control. *Nano Lett* 2014;14(8):4867–72.
- [12] Wang Y, Vallabhaneni A, Hu J, Qiu B, Chen YP, Ruan X. Phonon lateral confinement enables thermal rectification in asymmetric single-material nanostructures. *Nano Lett* 2014;14(2):592–6.
- [13] Zhang Z, Chen Y, Xie Y, Zhang S. Transition of thermal rectification in silicon nanocones. *Appl Therm Eng* 2016;102:1075–80.
- [14] Otey CR, Lau WT, Fan S. Thermal rectification through vacuum. *Phys Rev Lett* 2010;104(15):154301.
- [15] Francoeur M, Menguc MP. Role of fluctuational electrodynamics in near-field radiative heat transfer. *J Quant Spectrosc Radiat Transfer* 2008;109:280–93.
- [16] Bernardi MP, Milovich D, Francoeur M. Radiative heat transfer exceeding the blackbody limit between macroscale planar surfaces separated by a nanosize vacuum gap. *Nat Commun* 2016;7(1):12900.
- [17] Liu X, Shen J, Xuan Y. Pattern-free thermal modulator via thermal radiation between Van der Waals materials. *J Quant Spectrosc Radiat Transfer* 2017;200:100–7.
- [18] Bai Y, Jiang Y, Liu L. Enhanced near-field radiative heat transfer between a nanosphere and a hyperbolic metamaterial mediated by coupled surface phonon polaritons. *J Quant Spectrosc Radiat Transfer* 2015;158:61–8.
- [19] Shen S, Narayanaswamy A, Chen G. Surface phonon polaritons mediated energy transfer between nanoscale gaps. *Nano Lett* 2009;9(8):2909–13.
- [20] Basu S, Zhang ZM, Fu CJ. Review of near-field thermal radiation and its application to energy conversion. *Int J Energy Res* 2009;33(13):1203–32.
- [21] Wang XJ, Basu S, Zhang ZM. Parametric optimization of dielectric functions for maximizing nanoscale radiative transfer. *J Phys D* 2009;42(24):245403.
- [22] Fu CJ, Tan WC. Near-field radiative heat transfer between two plane surfaces with one having a dielectric coating. *J Quant Spectrosc Radiat Transfer* 2009;110(12):1027–36.
- [23] Narayanaswamy A, Shen S, Hu L, Chen X, Chen G. Breakdown of the Planck blackbody radiation law at nanoscale gaps. *Appl Phys A* 2009;96(2):357–62.
- [24] Dong J, Zhao J, Liu L. Long-distance near-field energy transport via propagating surface waves. *Phys Rev B* 2018;97(7):075422.
- [25] Shen S, Mavrokefalos A, Sambegoro P, Chen G. Nanoscale thermal radiation between two gold surfaces. *Appl Phys Lett* 2012;100(23):233114.
- [26] Didari A, Menguc MP. Near-field thermal emission between corrugated surfaces separated by nano-gaps. *J Quant Spectrosc Radiat Transfer* 2015;158:43–51.
- [27] Ashechik K, Mueller B, Krueger M. Heat radiation and transfer for point particles in arbitrary geometries. *Phys Rev B* 2017;96(15):155402.
- [28] Kim K, Song B, Fernandez-Hurtado V, Lee W, Jeong W, Cui L, et al. Radiative heat transfer in the extreme near field. *Nature* 2015;528(7582):387–91.
- [29] Fiorino A, Thompson D, Zhu L, Song B, Reddy P, Meyhofer E. Giant enhancement in radiative heat transfer in sub-30 nm gaps of plane parallel surfaces. *Nano Lett* 2018;18(6):3711–15.
- [30] Cui L, Jeong W, Fernandez-Hurtado C, Feist J, Garcia-Vidal FJ, Carlos Cuevas J, et al. Study of radiative heat transfer in angstrom and nanometre-sized gaps. *Nat Commun* 2017;8:14479.
- [31] Song B, Thompson D, Fiorino A, Ganjeh Y, Reddy P, Meyhofer E. Radiative heat conductances between dielectric and metallic parallel plates with nanoscale gaps. *Nat Nanotechnol* 2016;11(6):509–14.
- [32] Nikbakht M. Radiative heat transfer between core-shell nanoparticles. *J Quant Spectrosc Radiat Transfer* 2018;221:164–71.
- [33] Lim M, Song J, Kim J, Lee SS, Lee I, Lee BJ. Optimization of a near-field thermophotovoltaic system operating at low temperature and large vacuum gap. *J Quant Spectrosc Radiat Transfer* 2018;210:35–43.
- [34] Zhang Y, Wang C-H, Yi H-L, Tan H-P. Multiple surface plasmon polaritons mediated near-field radiative heat transfer between graphene/vacuum multilayers. *J Quant Spectrosc Radiat Transfer* 2018;221:138–46.
- [35] Kloppstech K, Koenne N, Biehs S-A, Rodriguez AW, Worbes L, Hellmann D, et al. Giant heat transfer in the crossover regime between conduction and radiation. *Nat Commun* 2017;8:14475.
- [36] Iizuka H, Fan S. Rectification of evanescent heat transfer between dielectric-coated and uncoated silicon carbide plates. *J Appl Phys* 2012;112(2):024304.
- [37] Basu S, Francoeur M. Near-field radiative transfer based thermal rectification using doped silicon. *Appl Phys Lett* 2011;98(11):113106.
- [38] Ben-Abdallah P, Biehs S-A. Phase-change radiative thermal diode. *Appl Phys Lett* 2013;103(19):191907.
- [39] Wang LP, Zhang ZM. Thermal rectification enabled by near-field radiative heat transfer between intrinsic silicon and a dissimilar material. *Nanoscale Microscale Thermophys Eng* 2013;17(4):337–48.
- [40] Zhu L, Otey CR, Fan S. Ultrahigh-contrast and large-bandwidth thermal rectification in near-field electromagnetic thermal transfer between nanoparticles. *Phys Rev B* 2013;88(18):184301.

- [41] Nefzaoui E, Joulain K, Drevillon J, Ezzahri Y. Radiative thermal rectification using superconducting materials. *Appl Phys Lett* 2014;104(10):103905.
- [42] Yang Y, Basu S, Wang L. Radiation-based near-field thermal rectification with phase transition materials. *Appl Phys Lett* 2013;103(16):163101.
- [43] Iizuka H, Fan S. Consideration of enhancement of thermal rectification using metamaterial models. *J Quant Spectrosc Radiat Transfer* 2014;148:156–64.
- [44] Joulain K, Ezzahri Y, Drevillon J, Rousseau B, De Sousa Meneses D. Radiative thermal rectification between SiC and SiO₂. *Opt Express* 2015;23(24):A1388–97.
- [45] Shen J, Liu X, He H, Wu W, Liu B. High-performance noncontact thermal diode via asymmetric nanostructures. *J Quant Spectrosc Radiat Transfer* 2018;211:1–8.
- [46] Ghanekar A, Ji J, Zheng Y. High-rectification near-field thermal diode using phase change periodic nanostructure. *Appl Phys Lett* 2016;109(12):123106.
- [47] Ghanekar A, Xiao G, Zheng Y. High contrast far-field radiative thermal diode. *Sci Rep* 2017;7(1):6339.
- [48] Fiorino A, Thompson D, Zhu L, Mittapally R, Biehs S-A, Bezencenet O, et al. A thermal diode based on nanoscale thermal radiation. *ACS Nano* 2018;12(6):5774–9.
- [49] Ito K, Nishikawa K, Iizuka H, Toshiyoshi H. Experimental investigation of radiative thermal rectifier using vanadium dioxide. *Appl Phys Lett* 2014;105(25):253503.
- [50] Zheng Z, Liu X, Wang A, Xuan Y. Graphene-assisted near-field radiative thermal rectifier based on phase transition of vanadium dioxide (VO₂). *Int J Heat Mass Transfer* 2017;109:63–72.
- [51] Huang J, Li Q, Zheng Z, Xuan Y. Thermal rectification based on thermochromic materials. *Int J Heat Mass Transfer* 2013;67:575–80.
- [52] Ghanekar A, Tian Y, Ricci M, Zhang S, Gregory O, Zheng Y. Near-field thermal rectification devices using phase change periodic nanostructure. *Opt Express* 2018;26(2):A209–AA18.
- [53] Elzouka M, Ndao S. Meshed doped silicon photonic crystals for manipulating near-field thermal radiation. *J Quant Spectrosc Radiat Transfer* 2018;204:56–62.
- [54] Gu W, Tang G-H, Tao W-Q. Thermal switch and thermal rectification enabled by near-field radiative heat transfer between three slabs. *Int J Heat Mass Transfer* 2015;82:429–34.
- [55] Xu G, Sun J, Mao H, Pan T. Surface plasmon-enhanced near-field thermal rectification in graphene-based structures. *J Appl Phys* 2018;124(18):183104.
- [56] Jia S, Fu Y, Su Y, Ma Y. Far-field radiative thermal rectifier based on nanostructures with vanadium dioxide. *Opt Lett* 2018;43(22):5619–22.
- [57] Tang L, Francoeur M. Photonic thermal diode enabled by surface polariton coupling in nanostructures. *Opt Express* 2017;25(24):A1043–A1A52.
- [58] Avanesian T, Hwang G. Adsorption-based thermal rectifier. In: ASME 2015 13th International Conference on Nanochannels, Microchannels, and Minichannels collocated with the ASME 2015 International Technical Conference and Exhibition on Packaging and Integration of Electronic and Photonic Microsystems: American Society of Mechanical Engineers; 2015. p. V001T04A24–V00VT04A24.
- [59] Hu J, Ruan X, Chen YP. Thermal conductivity and thermal rectification in graphene nanoribbons: a molecular dynamics study. *Nano Lett* 2009;9(7):2730–5.
- [60] Fu CJ, Zhang ZM. Nanoscale radiation heat transfer for silicon at different doping levels. *Int J Heat Mass Transfer* 2006;49(9–10):1703–18.
- [61] Olego D, Cardona M. Temperature dependence of the optical phonons and transverse effective charge in 3C-SiC. *Phys Rev B* 1982;25(6):3889–96.
- [62] Francoeur M, Menguc MP, Vaillon R. Local density of electromagnetic states within a nanometric gap formed between two thin films supporting surface phonon polaritons. *J Appl Phys* 2010;107(3):034313.
- [63] Rytov SM. Theory of electric fluctuations and thermal radiation. Bedford, MA: Air Force Cambridge Research Center; 1959.
- [64] Narayanaswamy A, Chen G. Thermal near-field radiative transfer between two spheres. *Phys Rev B* 2008;77(7):075125.
- [65] Kong J, Tsang L, Ding K. Scattering of electromagnetic waves, theories and applications, 1. New York: Wiley; 2000.
- [66] Landau L, Lifshitz E. Statistical physics. Reading, MA: Addison-Wesley; 1958.
- [67] Edalatpour S, Francoeur M. The Thermal Discrete Dipole Approximation (T-DDA) for near-field radiative heat transfer simulations in three-dimensional arbitrary geometries. *J Quant Spectrosc Radiat Transfer* 2014;133:364–73.
- [68] Edalatpour S, Francoeur M. Near-field radiative heat transfer between arbitrarily shaped objects and a surface. *Phys Rev B* 2016;94(4):045406.
- [69] Schmehl R. The coupled-dipole method for light scattering from particles on plane surfaces. Arizona State University, Dept of Mechanical and Aerospace Engineering; 1994. p. 18.
- [70] Edalatpour S, Cuma M, Trueax T, Backman R, Francoeur M. Convergence analysis of the thermal discrete dipole approximation. *Phys Rev E* 2015;91(6):063307.
- [71] Loomis JJ, Maris HJ. Theory of heat transfer by evanescent electromagnetic waves. *Phys Rev B* 1994;50(24):18517–24.
- [72] Sasihithlu K, Narayanaswamy A. Proximity effects in radiative heat transfer. *Phys Rev B* 2011;83(16):161406.
- [73] Loke VL, Menguc MP, Nieminen TA. Discrete-dipole approximation with surface interaction: computational toolbox for MATLAB. *J Quant Spectrosc Radiat Transfer* 2011;112(11):1711–25.
- [74] Dong J, Zhao J, Liu L. Radiative heat transfer in many-body systems: coupled electric and magnetic dipole approach. *Phys Rev B* 2017;95(12):125411.
- [75] Volokitin A, Persson B. Radiative heat transfer between nanostructures. *Phys Rev B* 2001;63(20):205404.
- [76] Bohren CF, Huffman DR. Absorption and scattering of light by small particles. John Wiley & Sons; 2008.
- [77] Zhang ZM. Nano/microscale heat transfer. McGraw-Hill; 2007.
- [78] Richter H, Wang Z, Ley L. The one phonon Raman spectrum in microcrystalline silicon. *Solid State Commun* 1981;39(5):625–9.
- [79] Murshed SMS, de Castro CAN. A critical review of traditional and emerging techniques and fluids for electronics cooling. *Renew Sust Energ Rev* 2017;78:821–33.